Editors' Suggestion

Unmasking the interior magnetic domain structure and evolution in Nd-Fe-B sintered magnets through high-field magnetic imaging of the fractured surface

David Billington,[1,2] Kentaro Toyoki,[1,2] Hiroyuki Okazaki,[1,2] Yoshinori Kotani,[1] Tomoki Fukagawa,[3] Takeshi Nishiuchi,[3] Satoshi Hirosawa,[2] and Tetsuya Nakamura[1,2,*]

[1]*Japan Synchrotron Radiation Research Institute, SPring-8, Sayo 679-5198, Japan*

[2]*Elements Strategy Initiative Center for Magnetic Materials (ESICMM), National Institute for Materials Science, Tsukuba 305-0047, Japan*

[3]*Magnetic Materials Research Laboratory, Hitachi Metals, Ltd., Kumagaya 360-8577, Japan*

(Received 1 August 2018; published 26 October 2018)

Conventional magnetic imaging techniques have observed magnetic domains in the polished surface of Nd-Fe-B sintered magnets, but the mechanical processing involved introduces numerous defects that facilitate the nucleation of reversed domains, thereby masking the interior domain structure. Here, we utilize high-field synchrotron x-ray magnetic circular dichroism microscopy to map the elemental and magnetic distributions in the polished and fractured surfaces of a Nd-Fe-B sintered magnet throughout its entire demagnetization process. As the applied field is varied, the domains in the fractured surface behave completely differently from those in the polished surface, thereby unmasking the interior domain structure and behavior. The area-averaged fractured surface coercivity is $\mu_0 H_c^{\mathrm{frac}} = 0.85\,\mathrm{T}$ which is much higher than the area-averaged polished surface coercivity, $\mu_0 H_c^{\mathrm{pol}} = 0.5\,\mathrm{T}$. Most of the local magnetic hysteresis loops are positively or negatively biased from the zero of the field axis. The highest coercivity grains, some of which exceed 2 T, are almost always located in the vicinity of strongly oppositely biased adjacent grains. This indicates that these oppositely biased grains are strongly influencing the magnetostatic field at the sample surface.

DOI: 10.1103/PhysRevMaterials.2.104413

I. INTRODUCTION

In a world with ever-increasing energy and environmental concerns, there is a significant demand for higher-performance permanent magnets for the next generation of green-energy applications such as electric vehicles and wind turbines [1–6]. One of the most desirable properties of a permanent magnet is a large coercivity, i.e., the field required to demagnetize the magnet. Since the coercivity is directly related to the nucleation of reversed magnetic domains and pinning of the domain walls, magnetic domain observations throughout the entire demagnetization process are essential. Currently, Nd-Fe-B sintered magnets represent the pinnacle of permanent magnet technology with the highest known maximum energy products, $(BH)_{\mathrm{max}}$ [7,8]. These materials have a granular structure primarily consisting of the main $Nd_2Fe_{14}B$ phase [9] and various Nd-rich subphases [10]. When optimally annealed, the coercivity is significantly enhanced, and this enhancement has been linked to the formation of thin, continuous, Nd-enriched grain boundary (GB) phases, which coat the $Nd_2Fe_{14}B$ grains [11–14]. Since the generation, structure, and evolution of magnetic domains is expected to be closely related to the distribution of crystalline and amorphous phases (and their respective magnetic properties), correlating the observed magnetic domains with the distribution of compositionally different phases that comprise the microstructure is also highly desirable.

An inevitable part of magnet preparation is surface cutting and/or polishing. Kerr microscopy [15–17], magnetic force microscopy [18], and photoelectron emission microscopy [19,20] have all observed magnetic domains in polished surfaces. However, the mechanical polishing these techniques require leads to significant degradation of the magnetic properties, especially the coercivity [21–23], because of the introduction of defects and the erosion of the GB phases [24]. These defects mainly come from oxidization and crystal dislocations and distortions which reduce the local magnetocrystalline anisotropy thereby lowering the field threshold for the nucleation of reversed magnetic domains and thus decreasing the coercivity [25–28]. On the other hand, when these materials are fractured, the GB phases remain [29] and the coercivity is maintained indicating that fracturing the surface minimizes the introduction of new defects because the main $Nd_2Fe_{14}B$ phase is protected and, therefore, magnetic domain observations of the fractured surface are representative of the interior magnetic state.

Unfortunately, imaging the magnetic domains in the fractured surface has proven to be extremely difficult primarily because the surface morphology is considerably different. To illustrate this, Fig. 1(a) shows scanning electron microscope (SEM) image of the polished surface, together with its corresponding height map as measured by a confocal microscope from two different viewpoints in (b) and (c), while Fig. 1(d) shows the SEM image of the fractured surface and (e) and (f) show its corresponding height map from two different viewpoints. Here, the polished surface is relatively flat with a standard height deviation of $\sigma_z^{\mathrm{pol}} = 0.07\,\mu\mathrm{m}$, while the fractured surface is much more irregular with $\sigma_z^{\mathrm{frac}} = 7\,\mu\mathrm{m}$.

*naka@spring8.or.jp

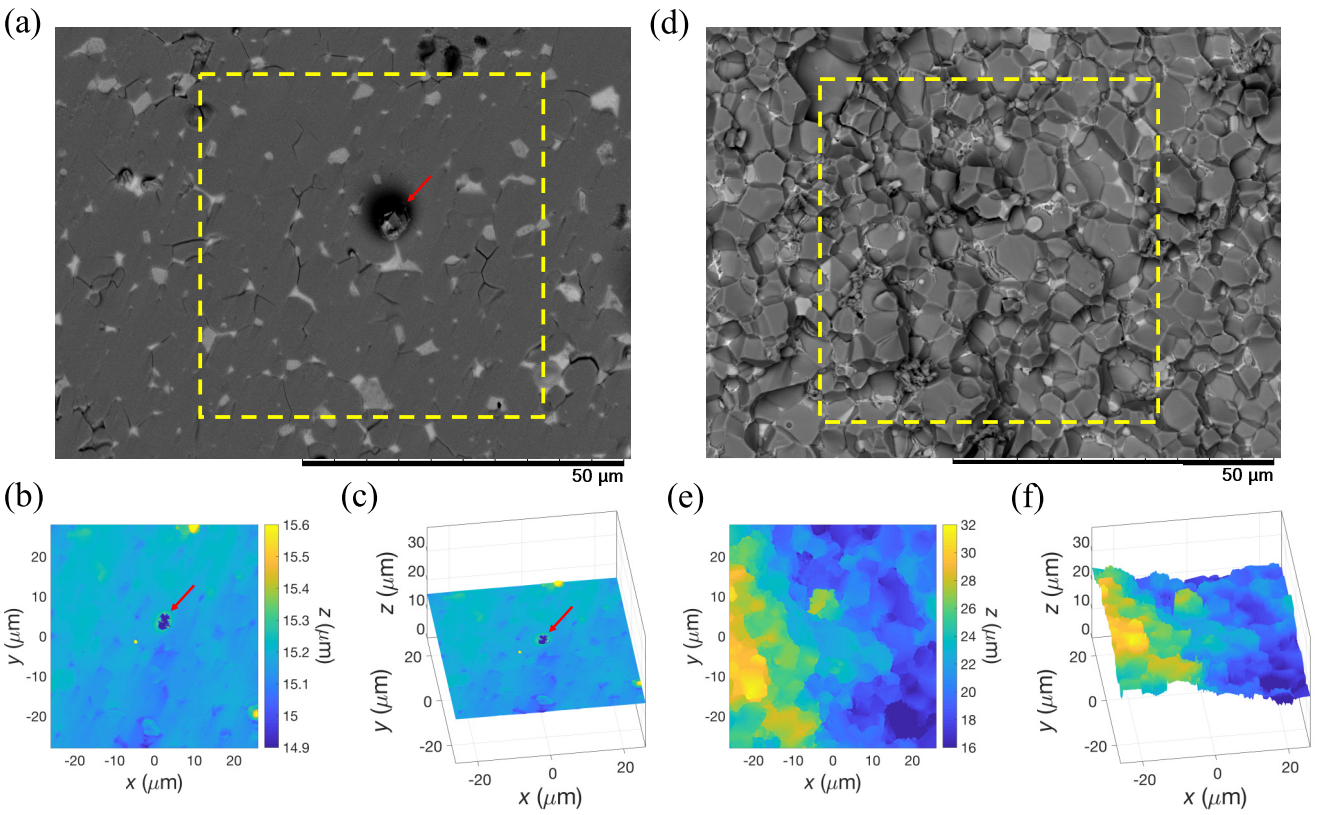

FIG. 1. SEM images and height maps of the polished and fractured surfaces. (a) SEM image of the polished surface. The scale bar is indicated below the image and the yellow square approximately indicates the area where the height maps and x-ray absorption images (shown later) were taken. (b),(c) Height maps of the polished surface as measured by a confocal microscope and plotted parallel to the magnetic easy axis and a different angle, respectively, to demonstrate the surface morphology. The color scale is the same in (b) and (c). (d)–(f) Same as (a)–(c), respectively, but for the fractured surface. The color scale is the same in (e) and (f), but is different from (b) and (c). Note that the SEM and confocal microscope measurements were made after the x-ray absorption microscopy measurements and the red arrows in (a)–(c) point to a contaminant on the polished surface that was not present during the x-ray absorption microscopy measurements.

A spin-polarized SEM has successfully observed magnetic domains in the fractured surface [29], but only small magnetic fields can be applied with this technique since it is electron beam based and larger magnetic fields adversely affect the electron microscopy lenses. More recently, magnetic domain generation and evolution in the fractured surface has been observed at the Nd L_2 edge with a scanning hard x-ray magnetic circular dichroism (XMCD) microscope [30]. However, their effective spatial resolution was relatively poor since the probing depth was about 2 μm and fields could only be applied up to about ± 2.2 T which is barely enough to completely saturate the magnet. What is required is a technique that can observe the fractured surface with much better spatial resolution and under much larger applied magnetic fields.

In this study, we have mapped the elemental and magnetic distributions in the polished and fractured surfaces of an optimally annealed, magnetically anisotropic, Cu-containing Nd-Fe-B (Nd-Fe-B-Cu) sintered magnet through magnetic field dependent x-ray absorption microscopy measurements with circularly polarized photons. This has allowed us to map the distribution of compositionally distinct phases in the polished and fractured surfaces by combining measurements at both the Fe L_3 and Nd M_4 edges. In order to gain a deeper understanding of the exterior and interior magnetization reversal processes we have determined the local magnetic hysteresis loops by performing magnetic field dependent Fe L_3 edge XMCD measurements on the polished and fractured surfaces, respectively, and these measurements have allowed us to map the local coercivities. Finally, combining the elemental and magnetic distributions has provided important insights into the local magnetic behavior and intergranular magnetic interactions.

II. EXPERIMENT

A. Sample preparation

The sample used in this study was cut from the same ingot that was used in previous studies [23]. The composition was $Nd_{30.6}Pr_{0.05}Fe_{67.4}B_{1.00}Dy_{0.01}Co_{0.00}Al_{0.05}Cu_{0.09}$ wt. % or $Nd_{13.7}Pr_{0.02}Fe_{77.9}B_{5.97}Dy_{0.00}Co_{0.00}Al_{0.12}Cu_{0.09}$ at. % as measured by inductively coupled plasma analysis (note that Al, Co, Pr, and Dy are impurities). After sintering at 1020 °C, the sample was annealed at 540 °C for 2 h. For the polished surface, the sample was cut to dimensions of about $1 \times 1 \times 5\,\text{mm}^3$ and polished, while the sample to be fractured was cut to dimensions of about $0.5 \times 0.5 \times 5\,\text{mm}^3$ (with the magnetic easy axis along the long dimension in both cases). For the polished sample, the sample was introduced to the ultrahigh vacuum (UHV) chamber of the x-ray absorption microscopy apparatus, before being sputtered with an Ar ion plasma in

order to remove the contaminated surface oxide layer. For the Ar ion sputtering, the acceleration voltage was 2 kV, the emission current was 10 mA, the incident angle was 45°, the Ar pressure was 6.7×10^{-3} Pa, and the duration was 30 min. This etched the sample surface by about 3 nm. For the fractured surface, the sample was fractured along a plane perpendicular to the magnetic easy axis under UHV and the x-ray absorption microscopy measurements were conducted *in situ*.

B. X-ray absorption microscopy

In this experiment, the absorption signals were recorded with the recently developed high-field scanning x-ray absorption microscope on BL25SU, SPring-8, by means of the total electron yield (TEY) method [31]. Importantly, this instrument has a focal depth of $\pm 5\mu$m from the focal point, a probing depth of 1.2 nm (at the Fe L_3 edge) giving a spatial resolution of about 100 nm, and is equipped with a superconducting magnet (with a maximum field of ± 8 T) thereby permitting investigations of the magnetic domains in polished and fractured surfaces of Nd-Fe-B sintered magnets throughout their entire demagnetization processes.

In x-ray absorption spectroscopy (XAS), the x-ray absorption spectrum is given by $\mu(E) = [\mu^+(E) + \mu^-(E)]/2$ and the XMCD spectrum is given by $\Delta\mu(E) = [\mu^+(E) - \mu^-(E)]$, where $\mu^+(E)$ and $\mu^-(E)$ represent the energy-dependent absorption of soft x-ray photons with positive and negative helicity, h^+ and h^-, respectively. When using the microscopy instrument, the energy is fixed at a chosen energy E, and the absorption is measured as a function of position (in x and y) on the sample, i.e., we measure

$$\mu_E^{\pm}(x, y) = \int \mu^{\pm}(E', x, y)\delta(E' - E)dE', \tag{1}$$

where the δ function represents the chosen (Gaussian) energy resolution. In this experiment, the energy resolution was set to $E/\Delta E = 3000$, where ΔE is the Gaussian full width at half maximum. The XAS and XMCD maps are then given by $\mu_E(x, y) = [\mu_E^+(x, y) + \mu_E^-(x, y)]/2$ and $\Delta\mu_E(x, y) = [\mu_E^+(x, y) - \mu_E^-(x, y)]$, respectively. In order to account for the nonlinear variation of the TEY signal with applied field [32], H_{ext}, the XMCD maps which give the magnetic domain structure are normalized by the XAS maps, i.e., we plot $\Delta\mu_E(x, y)/\mu_E(x, y)$. The data points in the magnetic hysteresis loops are then given by the area-averaged integral of the normalized XMCD maps, i.e., $\iint [\Delta\mu_E(x, y)/\mu_E(x, y)]dxdy/\iint dxdy$.

C. Composition mapping

For Nd-Fe-B sintered magnets, the ratio of Fe absorption relative to Nd can be used to understand the constituents of the polished and fractured surfaces. Therefore, in order to establish the distribution of Fe and Nd in the fractured surface, we determined the Fe/Nd absorption ratio, $A(x, y)$, given by

$$A(x, y) = \alpha \frac{\mu_{\text{Fe},L_3}(x, y) - \mu_{\text{Fe,pre-}L_3}(x, y)}{\mu_{\text{Nd},M_4}(x, y) - \mu_{\text{Nd,pre-}M_4}(x, y)}, \tag{2}$$

where α is a proportionality constant and $\mu_{\text{Fe},L_3}(x, y)$, $\mu_{\text{Fe,pre-}L_3}(x, y)$, $\mu_{\text{Nd},M_4}(x, y)$, and $\mu_{\text{Nd,pre-}M_4}(x, y)$ are the constant-energy, position-dependent x-ray absorption signals recorded at the Fe L_3 edge (707.9 eV), Fe L_3 pre-edge (704.0 eV), Nd M_4 edge (1000.4 eV), and Nd M_4 pre-edge (994.0 eV), respectively. In the determination of $A(x, y)$ from Eq. (2), the subtraction of $\mu_{\text{Fe,pre-}L_3}(x, y)$ from $\mu_{\text{Fe},L_3}(x, y)$ and $\mu_{\text{Nd,pre-}M_4}(x, y)$ from $\mu_{\text{Nd},M_4}(x, y)$ before the division is necessary to properly account for the background absorption signal. Therefore, a measurement of $A(x, y)$ takes eight scans; one scan for each helicity at each energy. If a $Nd_2Fe_{14}B$ grain in the $A(x, y)$ map has no GB coverage, either because of erosion during polishing or intragrain fracturing, it is possible to determine the proportionality constant α because A should be equal to the ratio of the number of Fe atoms to the number of Nd atoms, i.e., $A = 14/2 = 7$ for the exposed $Nd_2Fe_{14}B$ phase. By histogramming $A(x, y)$ and fitting a Gaussian function to the peak from the exposed $Nd_2Fe_{14}B$ phase, $A(x, y)$ can be normalized such that this peak lies at $A = 7$.

D. Local magnetic properties

For the local coercivity $H_c(x, y)$ and local magnetic bias $H_b(x, y)$ measurements, we define $H_c(x, y)$ as

$$H_c(x, y) = |H_+(x, y) - H_-(x, y)|/2, \tag{3}$$

and $H_b(x, y)$ as

$$H_b(x, y) = [H_+(x, y) + H_-(x, y)]/2, \tag{4}$$

where $H_+(x, y)$ and $H_-(x, y)$ are the position-dependent high and low fields where the normalized Fe L_3 edge XMCD signal, $\Delta\mu_{\text{Fe},L_3}(x, y)/\mu_{\text{Fe},L_3}(x, y)$, is zero, respectively.

III. RESULTS AND DISCUSSION

In order to determine the composition of the polished and fractured surfaces of the Nd-Fe-B-Cu sintered magnet, we have first measured the Fe L_3 and Nd M_4 edge x-ray absorption maps, and determined their quotient. In the following, the identification of the various phases has been confirmed by scanning electron microscope with energy dispersive x-ray (SEM-EDX) microscopy discussed in the Supplemental Material and shown in Fig. S1 [33].

Figure 2(a) shows the polished surface Fe to Nd absorption ratio map, $A(x, y)$ [see Eq. (2)], and Fig. 2(b) shows a histogram of the $A(x, y)$ map. Here, $A(x, y)$ is largely covered by the exposed $Nd_2Fe_{14}B$ phase (red, $A \approx 7$) with a smaller amount of Nd-rich regions (blue, $A \approx 0$). Furthermore, the B-rich $Nd_5Fe_{18}B_{18}$ ($Nd_{1.1}Fe_4B_4$) phase [34] ($2.7 \lesssim A \lesssim 3.3$, light blue to white) is also observable. The $A(x, y)$ map for the fractured surface is shown in Fig. 2(c), and 2(d) shows a histogram of the $A(x, y)$ map. As can be seen, the composition of the fractured surface is markedly different from the polished surface. For the fractured surface, a small number of exposed $Nd_2Fe_{14}B$ grains are visible (red, $A \approx 7$), as are the Nd-rich phases (blue, $A \approx 0$). The rest of the image consists of large regions with intermediate A values (light blue to white, $2.5 \lesssim A \lesssim 5.5$) which comes from the main $Nd_2Fe_{14}B$ grains coated with the Nd-rich GB phases, and possibly also some of the B-rich $Nd_5Fe_{18}B_{18}$ phase, although

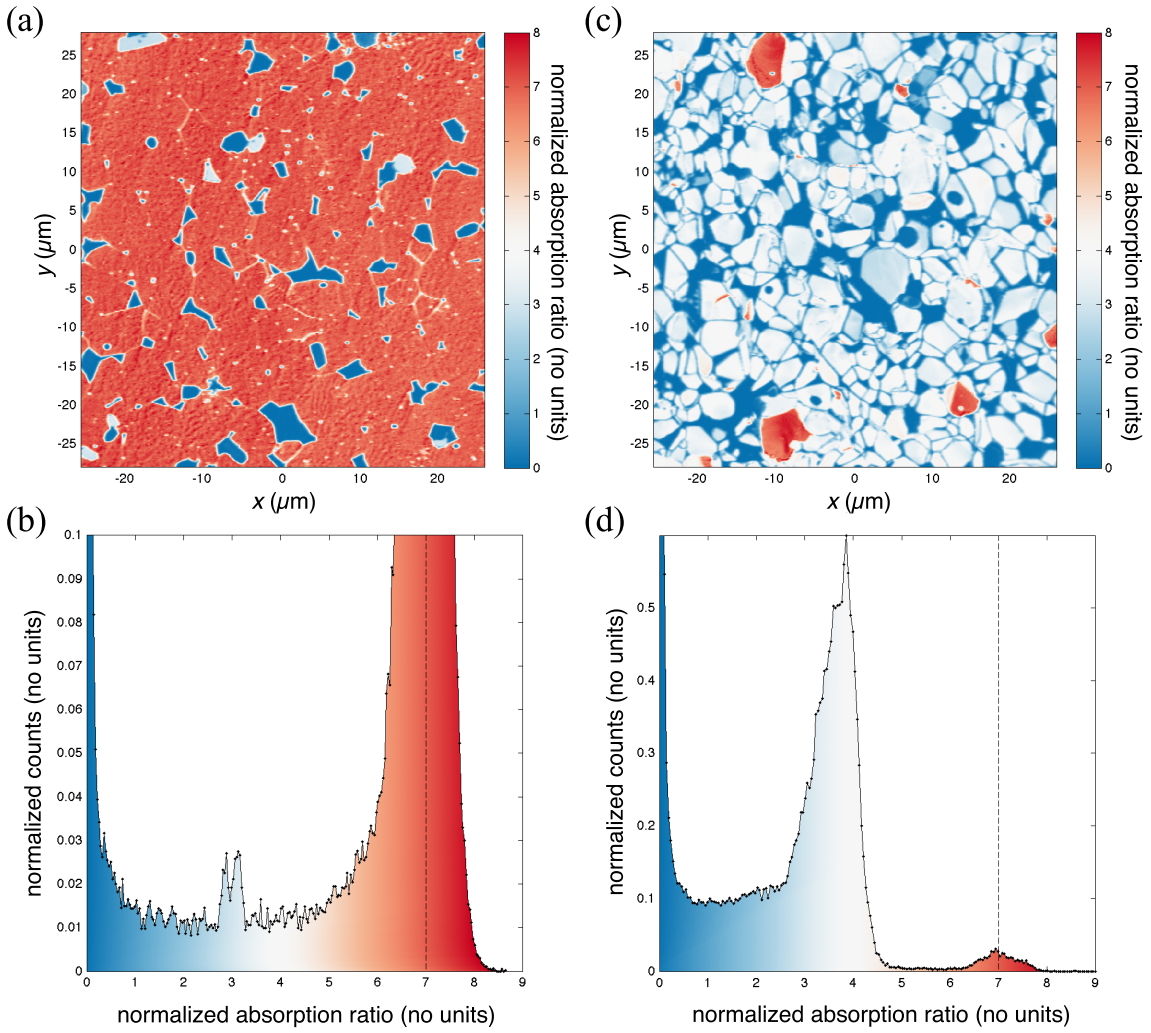

FIG. 2. Composition mapping of the polished and fractured surfaces. (a) Normalized absorption ratio map, $A(x, y)$, of the polished surface [as defined in Eq. (2)], which is proportional to the quotient of the background-corrected Fe L_3 edge and Nd M_4 edge absorption maps. (b) Histogram of the image shown in (a). (c) Same as (a), but for the fractured surface. (d) Histogram of the image shown in (c).

these features strongly overlap making the identification of the B-rich phase extremely difficult for the fractured surface. The observed differences between the polished and fractured surface $A(x, y)$ maps indicate that the GB phases have been completely removed by the polishing process.

Having mapped the distribution of phases in the polished and fractured surfaces, we performed Fe L_3 edge XMCD measurements under various applied magnetic fields around the major hysteresis loop. As part of the Supplemental Material [33], we have included videos of the magnetic domain images measured in the polished and fractured surfaces showing where the reversed magnetic domains are nucleated and how they propagate.

In the polished surface, a multiple-domain state is formed when the applied magnetic field becomes close to the area-averaged coercivity, $|\mu_0 H_c^{\mathrm{pol}}| = 0.5\,\mathrm{T}$, of the descending branch. Figures 3(a) and 3(b) show the polished surface magnetic domain images taken just above and below H_c^{pol}. Here, large regions are covered by the mazelike domain pattern. In response to changing H_{ext}, the domain walls easily move because of the fine balance between the external field and the magnetostatic stray field at the surface. In contrast, the demagnetization process of the fractured surface occurs grain by grain where most of the grains completely reverse their magnetization, without exhibiting the mazelike domain pattern of the multiple-domain state that is seen in the polished surface. Figures 3(d) and 3(e) show the fractured surface magnetic domain images taken just above and below the area-averaged coercivity, $|\mu_0 H_c^{\mathrm{frac}}| = 0.85\,\mathrm{T}$, of the descending branch. Here, very few grains exhibit multiple domains, demonstrating the grain by grain nature of the magnetization reversal. Near the coercivity, the reversed magnetic domains extend over multiple whole grains both in the (x, y) plane and out of the plane (z direction) as demonstrated by the cascade propagation observed previously [15].

Since the Fe L_3 edge XMCD maps were all taken from the same sample areas, we are able to extract the local magnetic hysteresis loops for each pixel of area $150 \times 150\,\mathrm{nm}^2$. From the $A(x, y)$ maps, we can then select the pixels which lie within some range of A values in order to plot the local magnetic hysteresis loops for compositionally different regions. Figures 3(c) and 3(f) show the area-averaged

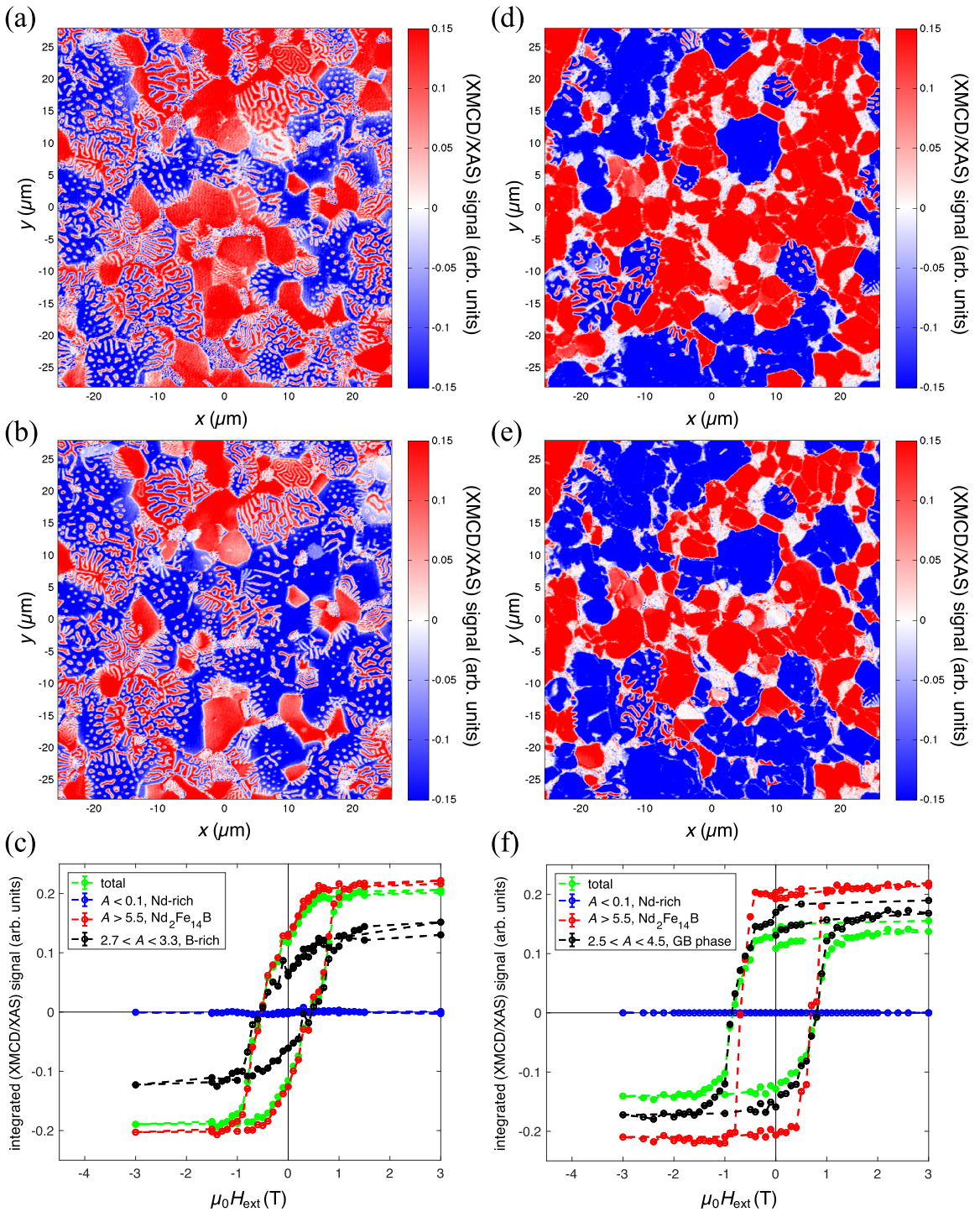

FIG. 3. Magnetic domain images and composition-dependent hysteresis loops from the polished and fractured surfaces. (a),(b) Polished surface Fe L_3 edge XMCD maps taken just above and below its coercivity H_c^{pol}, respectively. (c) Hysteresis loop taken from compositionally different regions of the polished surface, as determined by their $A(x, y)$ value in Fig. 2(a). The legends indicate the range of A values used to determine each hysteresis loop. (d),(e) Same as (a) and (b), respectively, but for the fractured surface and its coercivity, H_c^{frac}. (f) Same as (c), but the compositionally different regions are determined from their $A(x, y)$ value in Fig. 2(c). The area shown in (a) and (b) is the same as Fig. 2(a), and the area shown in (d) and (e) is the same as Fig. 2(c).

composition-dependent magnetic hysteresis loops taken from the polished and fractured surfaces, respectively. The polished surface is magnetically softer than the fractured surface. In the polished surface, the magnetic hysteresis loops of both the main $Nd_2Fe_{14}B$ phase and the B-rich phase essentially track the total area-averaged curve. In the fractured surface, the magnetic hysteresis loop from the exposed main $Nd_2Fe_{14}B$ phase grains is almost square, suggesting that their magnetic

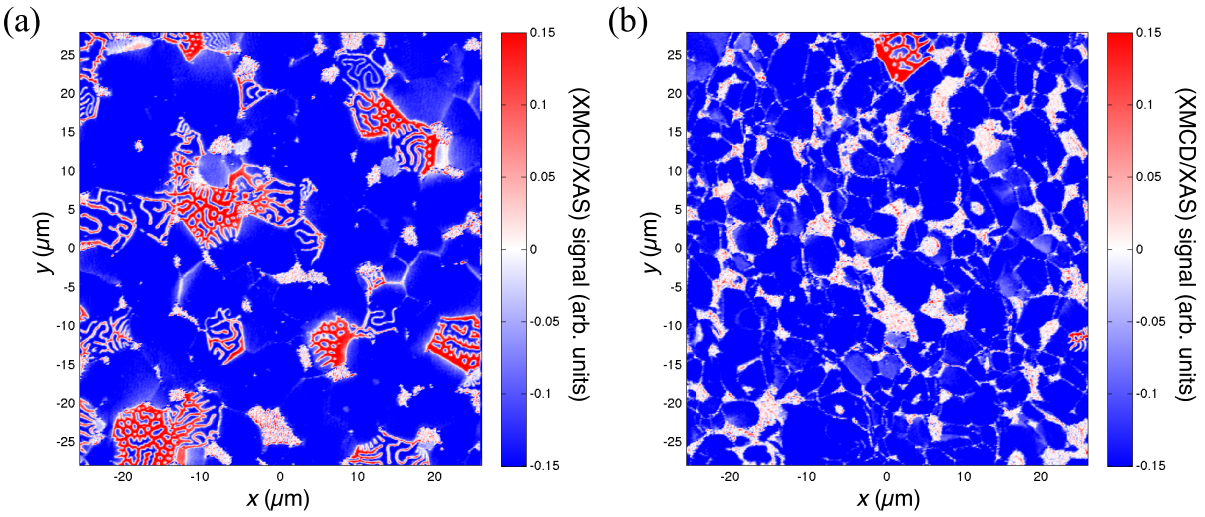

FIG. 4. Magnetic domain images from the polished and fractured surfaces in the remanent state. (a),(b) Polished and fractured surface Fe L_3 edge XMCD maps, respectively, both taken at $\mu_0 H_{\text{ext}} = 0.0\,\text{T}$ after being saturated at $\mu_0 H_{\text{ext}} = -3.0\,\text{T}$.

easy axis is well aligned with the x-ray incidence direction, possibly because of an increased propensity for cleaving in the plane perpendicular to the easy axis. Interestingly, the average coercivity of the GB-coated main phase grains is slightly higher than that of the exposed main phase, possibly indicating that the magnetic anisotropy of the GB-coated main phase grains is larger because it is not exposed and it is relatively defect-free, as suggested by first-principles calculations [25].

Figures 4(a) and 4(b) show the polished and fractured surface Fe L_3 edge XMCD maps, respectively, at remanence ($\mu_0 H_{\text{ext}} = 0.0\,\text{T}$) after being saturated at $\mu_0 H_{\text{ext}} = -3.0\,\text{T}$. Here, significant regions of the polished surface already exhibit the mazelike domain patterns, while only sparsely separated regions of the fractured surface exhibit reversed domains. Considering that the polished surface essentially sits directly on top of the fractured surface, and that both images are taken with zero applied field, it is clear that there has to be very little connection between the domains in the (out of plane, z direction) layers below. This means that the magnetic domain behavior of the exposed layer of grains at the polished surface seems to be independent of the layers of grains below, and unquestionably demonstrates that magnetic domain observations of the polished surface are not representative of the interior magnetic state.

Having determined the area-averaged composition-dependent magnetic hysteresis loops, we now examine the local coercivities and local magnetic biases of the polished and fractured surfaces. Figures 5(a) and 5(b) show $\mu_0 H_c(x, y)$ and $\mu_0 H_b(x, y)$, respectively, for the polished surface, and Figs. 5(d) and 5(e) show $\mu_0 H_c(x, y)$ and $\mu_0 H_b(x, y)$, respectively, for the fractured surface. In the polished surface, the mazelike domain patterns of the multiple-domain state observed near the coercivity are clearly imprinted on $H_c(x, y)$ and $H_b(x, y)$. Interestingly, it is possible to make out the individual grains in $H_c(x, y)$, whereas this was not possible from the absorption ratio map, $A(x, y)$, in Fig. 2(a). This indicates that, although the GB phases has been removed from the surface, there is a significant pinning force between adjacent $Nd_2Fe_{14}B$ grains where the coercivity enhancing GB phases are still present. It is clearly obvious that the polished surface has much lower field thresholds for the nucleation of reversed magnetic domains than the fractured surface. In both the polished and the fractured surface, some grains have significantly higher coercivities than their respective total-area averages. These higher-coercivity grains tend to have smaller than average sizes, as expected. By comparing the locations of these higher-coercivity grains in the $H_c(x, y)$ maps with their corresponding $H_b(x, y)$ maps, it can be seen that the higher-coercivity grains almost always lie close to oppositely biased pairs of grains, which appear as light-blue/orange in the polished surface $H_b(x, y)$ map, and red/blue in the fractured surface $H_b(x, y)$ map. Figures 5(c) and 5(f) show hysteresis loops taken from individual grains in the polished surface [labeled 1–4 in Fig. 5(c)] and the fractured surface [labeled 1–3 in Fig. 5(f)], respectively. These oppositely biased pairs are able to stabilize some of the nearby grains from reversing their magnetization up to much higher fields than the total-area-average coercivity, indicating that they are strongly interacting with the local magnetic field at the sample surface.

IV. CONCLUSIONS

In conclusion, x-ray absorption maps at different energies have allowed us to map the different phases in the Nd-Fe-B sintered magnet, and XMCD maps taken at various magnetic fields have allowed us to visualize the different magnetization reversal processes in the polished and fractured surfaces. The fractured surface, in which the coercivity is close to the bulk value, showed completely different magnetic domain behavior to the polished surface; for small changes in applied field the domain walls are able to travel through multiple whole grains. The mazelike multiple-domain structure in the polished surface reflects the reduced magnetic anisotropy, as evidenced by the narrow domain widths, and this is clearly a

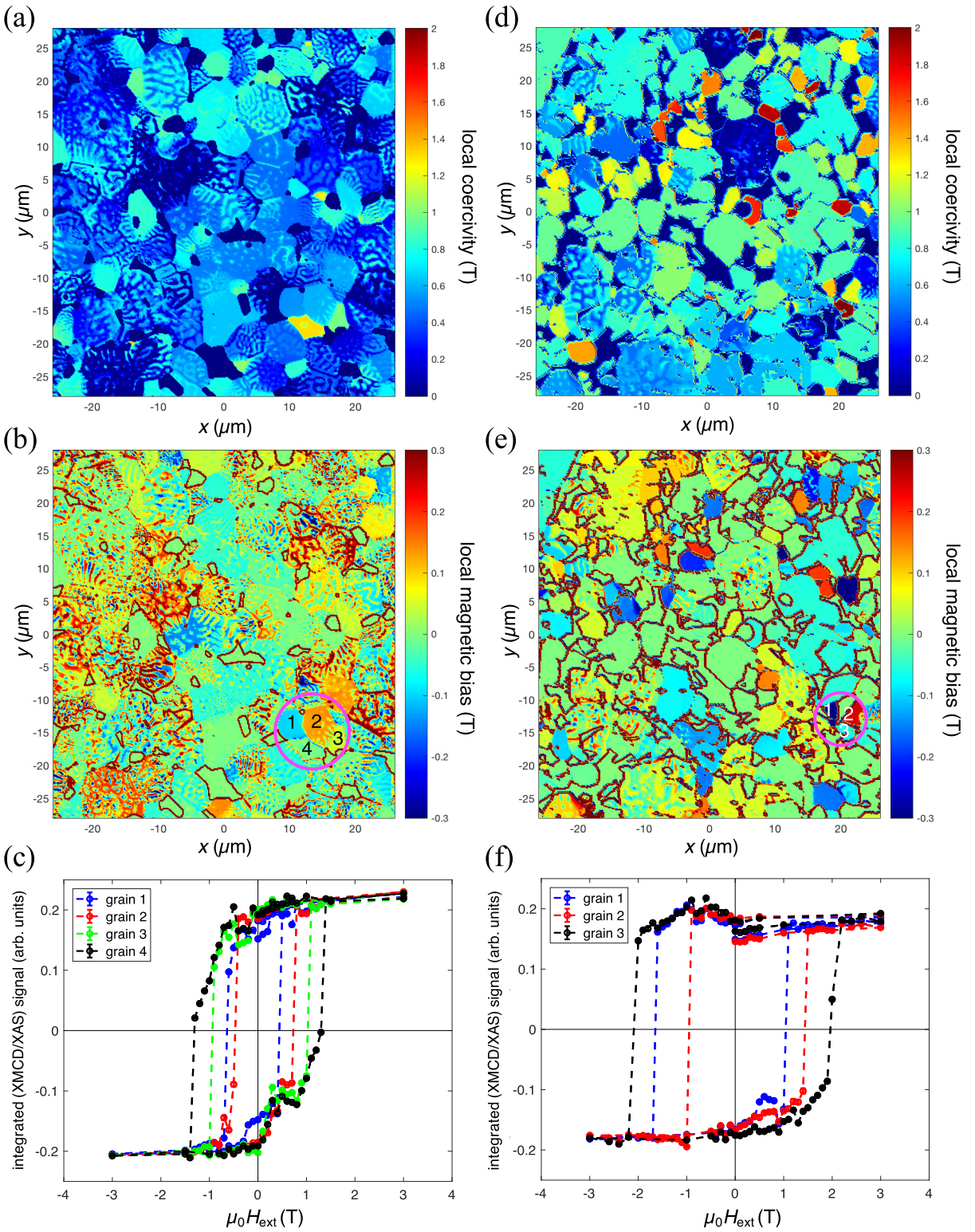

FIG. 5. Local coercivities and local magnetic biases of the polished and fractured surfaces. (a),(b) Local coercivity and local magnetic bias, $\mu_0 H_c(x, y)$ and $\mu_0 H_b(x, y)$, of the polished surface, as defined in Eqs. (3) and (4), respectively. The magenta circle in (b) encloses a cluster of grains labeled 1–4. (c) Local hysteresis loops for the grains labeled 1–4 in (b). (d),(e) Same as (a) and (b), respectively, but for the fractured surface. The magenta circle in (e) encloses a cluster of grains labeled 1–3. (f) Local hysteresis loops for the grains labeled 1–3 in (e). The area shown in (a) and (b) is the same as Fig. 2(a), and the area shown in (d) and (e) is the same as Fig. 2(c). The color scale is the same in (a) and (d), but is different from (b) and (e).

consequence of the surface damage. The difference between the polished and fractured surface domain structure at remanence demonstrates that most of the magnetic domains in the exposed layer of grains at the polished surface have to be disconnected from the domains in the layers of grains below. This indicates that the fractured surface displays the real magnetic domain structure in the interior of the magnet. Combining the XMCD maps with the composition analysis gives us the hysteresis loops from compositionally different regions. From the XMCD maps we have determined the local coercivity and local magnetic bias. The grains with the highest coercivities are almost always located in the vicinity of strongly oppositely biased pairs of grains indicating that these pairs strongly influence the local magnetic field at the sample surface and are able to stabilize certain grains from demagnetization up to much larger applied magnetic fields.

ACKNOWLEDGMENTS

The x-ray absorption microscopy experiment was performed with the approval of the Japan Synchrotron Radiation Research Institute (JASRI), Proposals No. 2014B1008, No. 2015A1009, No. 2015B1016, No. 2016A1008, No. 2016B1009, and No. 2017A1022. The Elements Strategy Initiative Center for Magnetic Materials (ESICMM) is funded by the Ministry of Education, Culture, Sports, Science and Technology (MEXT). The authors would also like to thank K. Hono, S. Okamoto, and M. Takata for invaluable discussions.

[1] O. Gutfleisch, M. A. Willard, E. Brück, C. H. Chen, S. G. Sankar, and J. P. Liu, Adv. Mater. **23**, 821 (2011).
[2] J. Coey, Scr. Mater. **67**, 524 (2012), viewpoint Set No. 51: Magnetic Materials for Energy.
[3] K. Hono and H. Sepehri-Amin, Scr. Mater. **67**, 530 (2012), viewpoint Set No. 51: Magnetic Materials for Energy.
[4] L. H. Lewis and F. Jiménez-Villacorta, Metall. Mater. Trans. A **44**, 2 (2013).
[5] S. Hirosawa, J. Magn. Soc. Jpn. **39**, 85 (2015).
[6] K. S. Stegen, Energy Policy **79**, 1 (2015).
[7] M. Sagawa, S. Fujimura, N. Togawa, H. Yamamoto, and Y. Matsuura, J. Appl. Phys. **55**, 2083 (1984).
[8] M. Sagawa, S. Hirosawa, H. Yamamoto, S. Fujimura, and Y. Matsuura, Jpn. J. Appl. Phys. **26**, 785 (1987).
[9] J. F. Herbst, Rev. Mod. Phys. **63**, 819 (1991).
[10] N. Tsuji, H. Okazaki, W. Ueno, Y. Kotani, D. Billington, A. Yasui, S. Kawaguchi, K. Sugimoto, K. Toyoki, T. Fukagawa, T. Nishiuchi, Y. Gohda, S. Hirosawa, K. Hono, and T. Nakamura, Acta Mater. **154**, 25 (2018).
[11] R. K. Mishra, J. K. Chen, and G. Thomas, J. Appl. Phys. **59**, 2244 (1986).
[12] F. Vial, F. Joly, E. Nevalainen, M. Sagawa, K. Hiraga, and K. Park, J. Magn. Magn. Mater. **242-245**, 1329 (2002).
[13] W. Li, T. Ohkubo, and K. Hono, Acta Mater. **57**, 1337 (2009).
[14] T. Sasaki, T. Ohkubo, and K. Hono, Acta Mater. **115**, 269 (2016).
[15] M. Soderžnik, H. Sepehri-Amin, T. Sasaki, T. Ohkubo, Y. Takada, T. Sato, Y. Kaneko, A. Kato, T. Schrefl, and K. Hono, Acta Mater. **135**, 68 (2017).
[16] M. Takezawa, H. Ogimoto, Y. Kimura, and Y. Morimoto, J. Appl. Phys. **115**, 17A733 (2014).
[17] K. Khlopkov, O. Gutfleisch, D. Eckert, D. Hinz, B. Wall, W. Rodewald, K.-H. Müller, and L. Schultz, J. Alloys Compd. **365**, 259 (2004).
[18] T. Yamaoka, H. Tsujikawa, S. Hasumura, K. Andou, M. Shigeno, A. Ito, and H. Kawamura, Microsc. Today **22**, 12 (2014).
[19] S. Yamamoto, M. Yonemura, T. Wakita, K. Fukumoto, T. Nakamura, T. Kinoshita, Y. Watanabe, F. Z. Guo, M. Sato, T. Terai, and T. Kakeshita, Mater. Trans. **49**, 2354 (2008).
[20] R. Yamaguchi, K. Terashima, K. Fukumoto, Y. Takada, M. Kotsugi, Y. Miyata, K. Mima, S. Komori, S. Itoda, Y. Nakatsu, M. Yano, N. Miyamoto, T. Nakamura, T. Kinoshita, Y. Watanabe, A. Manabe, S. Suga, and S. Imada, IBM J. Res. Dev. **55**, 12 (2011).
[21] S. Hirosawa, K. Tokuhara, and M. Sagawa, Jpn. J. Appl. Phys. **26**, L1359 (1987).
[22] T. Fukagawa and S. Hirosawa, Scr. Mater. **59**, 183 (2008).
[23] T. Nakamura, A. Yasui, Y. Kotani, T. Fukagawa, T. Nishiuchi, H. Iwai, T. Akiya, T. Ohkubo, Y. Gohda, K. Hono, and S. Hirosawa, Appl. Phys. Lett. **105**, 202404 (2014).
[24] K. Kobayashi, M.-H. Nakamura, and K. Urushibata, J. Appl. Phys. **117**, 173909 (2015).
[25] H. Tsuchiura, T. Yoshioka, and P. Novák, IEEE Trans. Magn. **50**, 2105004 (2014).
[26] Y. Toga, T. Suzuki, and A. Sakuma, J. Appl. Phys. **117**, 223905 (2015).
[27] T. Woodcock, Y. Zhang, G. Hrkac, G. Ciuta, N. Dempsey, T. Schrefl, O. Gutfleisch, and D. Givord, Scr. Mater. **67**, 536 (2012), viewpoint Set No. 51: Magnetic Materials for Energy.
[28] G. Hrkac, T. Woodcock, K. Butler, L. Saharan, M. Bryan, T. Schrefl, and O. Gutfleisch, Scr. Mater. **70**, 35 (2014).
[29] T. Kohashi, K. Motai, T. Nishiuchi, and S. Hirosawa, Appl. Phys. Lett. **104**, 232408 (2014).
[30] M. Suzuki, A. Yasui, Y. Kotani, N. Tsuji, T. Nakamura, and S. Hirosawa, Acta Mater. **106**, 155 (2016).
[31] Y. Kotani, Y. Senba, K. Toyoki, D. Billington, H. Okazaki, A. Yasui, W. Ueno, H. Ohashi, S. Hirosawa, Y. Shiratsuchi, and T. Nakamura, J. Synchrotron Radiat. **25**, 1444 (2018).
[32] E. Goering, A. Fuss, W. Weber, J. Will, and G. Schütz, J. Appl. Phys. **88**, 5920 (2000).
[33] See Supplemental Material at http://link.aps.org/supplemental/10.1103/PhysRevMaterials.2.104413 for composition analysis of the polished surface by SEM-EDX microscopy and videos of the magnetic domain images measured in the polished and fractured surfaces.
[34] D. Givord, J. Moreau, and P. Tenaud, Solid State Commun. **55**, 303 (1985).